

Sensitivity of the Astrometric Technique in Detecting Outer Planets

J. A. Eisner & S. R. Kulkarni

Palomar Observatory 105-24, California Institute of Technology, Pasadena, CA 91125
jae@astro.caltech.edu, srk@astro.caltech.edu

ABSTRACT

With the advent of optical interferometers that will be coming online in the next decade, radial velocity searches for extra-solar planets will be complemented by high angular resolution astrometric measurements. In this paper, we explore the sensitivity of the astrometric technique, and develop an analytical understanding of the sensitivity in the regime where the orbital period is longer than the time-baseline of the survey. As in an earlier paper that dealt with the radial velocity technique, our analysis of the astrometric technique utilizes both the orbital amplitude and phase.

1. Introduction

Radial velocity surveys of nearby stars have produced spectacular discoveries of extra-solar planets over the past two decades (see Marcy, Cochran & Mayor 2000). As these searches continue into the next decade, they will be supplemented by high angular resolution searches for the astrometric signatures of planetary orbits (e.g. Danner & Unwin 1999; van Belle et al. 1998; Horner et al. 1999). While radial velocity (RV) technique works by detecting the reflex acceleration of the star due to the orbital motion of the companion, astrometric technique detects the apparent reflex motion of the star on the sky. In a previous paper (Eisner & Kulkarni 2001, hereafter EK2001), we examined the RV technique in detail, paying particular attention to the regime where the time-baseline of the observations is shorter than the orbital period of the planet. This regime is interesting because while the longest baseline of current RV surveys is ~ 12 years, one expects giant planets to form in the colder regions of the proto-planetary nebula, and thus we expect such objects to possess periods of many years to centuries (Boss 1995). While RV technique is most sensitive to short-period, close-in planets, astrometric technique obtains optimal sensitivity to long-period massive planets expected from current theories. Moreover, in EK2001, we demonstrated that one can achieve a significant improvement in sensitivity (over current methods) if the orbital amplitude *and phase* are included in the analysis.

In this paper, we develop an analytical understanding of the sensitivity of astrometric technique in this so-called “long-period regime”, and address the issues of detection and detection efficiency. To the best of our knowledge, the last authors who dealt with the sensitivity of the astrometric method were Black & Scargle (1982), who used a periodogram approach (Black & Scargle 1982). As in EK2001, we will argue below that a least-squares approach is preferable to the periodogram. Essentially, the least-squares approach (in contrast to the periodogram method) offers the most general approach, and requires no modification in the long-period regime.

The plan of the paper is as follows. First, we address the case of edge-on orbits in §2. In §2.1, we summarize the basic equations and describe the least-squares approach in §2.2. In §2.3 we provide analytical estimates for obtaining a detection in the absence of any signal, and in §2.4 we obtain estimates for minimum detectable signals in the presence of noise. We repeat this analysis for the case of face-on orbits in §3 and for orbits with general inclination angles in §4. We conclude in §5.

2. Edge-On Orbits

2.1. Basic Equations

We will assume circular orbits throughout this discussion, and we will neglect the effect of annual parallax. The astrometric signature of an edge-on circular orbit is given by

$$\theta(t) = \mathcal{A} \sin \left(\frac{2\pi t}{\tau} + \phi \right) + \lambda t + \mu, \quad (1)$$

where t is the time; λ and μ are the proper motion and position offset of the planetary system, respectively; and

$$\mathcal{A} = \frac{M_p}{D} \left(\frac{G\tau^2}{4\pi^2 M_*^2} \right)^{\frac{1}{3}}. \quad (2)$$

Here, D is the distance to the system, M_* is the mass of the star, and M_p is the mass of the planet. Thus, we can express the sensitivity (defined as the minimum-mass planet that can be detected) of the astrometric technique in terms of the amplitude of the astrometric orbital signature:

$$M_p = D\mathcal{A} \left(\frac{4\pi^2 M_*^2}{G\tau^2} \right)^{\frac{1}{3}}. \quad (3)$$

However, it is more difficult to identify planets with long periods than Equation 3 might suggest. In the so-called “long-period regime”, the total baseline of the observations is less

than the orbital period of the planet, and thus we only observe some fraction of the full orbital amplitude. Thus the sensitivity is expected to critically depend on the orbital phase. As we will show explicitly below, astrometric technique (applied to an edge-on orbit) will be the most sensitive when the orbital curvature is maximal (i.e. $\phi = [n + 1/2]\pi$). In contrast, when the orbital phase is close to $n\pi$ (i.e. a pure sine wave), the lack of orbital curvature makes it difficult to distinguish the signal from the unknown proper motion of the system.

2.2. Least Squares Fitting of Sinusoids

The signal analysis for the astrometric technique consists of fitting the observations to the model specified in Equation 1. As noted by several authors (e.g. Scargle 1982; Nelson & Angel 1998; Eisner & Kulkarni 2001) the most optimal fitting is obtained by using the technique of least-squares. First, we derive a linear model equation from Equation 1:

$$\theta(t) = \mathcal{A}_c \cos(\omega t) + \mathcal{A}_s \sin(\omega t) + \lambda t + \mu. \quad (4)$$

Here, $\mathcal{A}_c = \mathcal{A} \sin \phi$, $\mathcal{A}_s = \mathcal{A} \cos \phi$. Black & Scargle (1982) estimated μ and λ first and then applied periodogram analysis to the residual data (i.e. with contributions from μ and λ subtracted). However, as discussed in EK2001, it is necessary to determine all of the parameters simultaneously, especially in the long-period regime.

Using Equation 4 as our physical model, we perform the following analysis to search for a signal in a data set. The parameters of the data set are as follows: the duration of the survey is T_0 , $\theta'(t_j)$ is the measured astrometric offset at epoch t_j , and n_0 is the number of measured epochs. With no loss of generality, we let the time go from $t = -T_0/2$ to $T_0/2$. To find the four unknowns, \mathcal{A}_c , \mathcal{A}_s , λ , and μ , we minimize

$$X^2 = \sum_{j=0}^{n_0-1} [\theta'(t_j) - \mathcal{A}_c \cos(\omega t_j) - \mathcal{A}_s \sin(\omega t_j) - \lambda t_j - \mu]^2 \quad (5)$$

with respect to \mathcal{A}_c , \mathcal{A}_s , λ , and μ . Here, $\omega = 2\pi/\tau$, where τ is the orbital period. This yields a matrix equation for the four unknowns, which must be solved numerically in the general case. However, in the short-period regime where we observe many orbital cycles, many of the summations will average to zero, and this matrix equation will become approximately diagonal. In this case, the fit parameters are given by

$$\mathcal{A}_c = \frac{2}{n_0} \sum_{j=0}^{n_0-1} \theta'(t_j) \cos(\omega t_j), \quad (6)$$

$$\mathcal{A}_s = \frac{2}{n_0} \sum_{j=0}^{n_0-1} \theta'(t_j) \sin(\omega t_j), \quad (7)$$

$$\lambda = \frac{\sum_{j=0}^{n_0-1} \theta'(t_j) t_j}{\sum_{j=0}^{n_0-1} t_j^2}, \quad (8)$$

$$\mu = \frac{1}{n_0} \sum_{j=0}^{n_0-1} \theta'(t_j). \quad (9)$$

2.3. Type I Errors

Type I errors describe the probability that a high amplitude will be obtained even when no signal is present in the data. We assess the statistics of Type I errors, assuming that our data set consists of Gaussian noise with a mean of zero and a standard deviation of σ_0 .

2.3.1. Short-Period Regime

From Equations 6–9, we see that \mathcal{A}_c , \mathcal{A}_s , λ , and μ are sums of Gaussian variables, and thus by the Gaussian addition theorem, the four derived parameters must also be Gaussian. Specifically, \mathcal{A}_c and \mathcal{A}_s obey a Gaussian distribution with a mean of zero and a variance of

$$\sigma^2 = \frac{2\sigma_0^2}{n_0}, \quad (10)$$

where n_0 is the number of measurements. Denoting by A_{1s} the value of $|\mathcal{A}_c|$ (or $|\mathcal{A}_s|$) that is exceeded in 1% of cases, we note that

$$A_{1s} = 2.61\sigma = 3.69 n_0^{-1/2} \sigma_0. \quad (11)$$

From Equation 9, we see that μ obeys a Gaussian distribution with zero mean and a variance of σ_0^2/n_0 . Denoting by μ_{1s} the value of $|\mu|$ that is exceeded in 1% of cases,

$$\mu_{1s} = 2.61\sigma = 2.61 n_0^{-1/2} \sigma_0. \quad (12)$$

Since the statistics of λ are somewhat more complicated, we will infer the approximate value of λ_{1s} from the value of μ_{1s} :

$$\lambda_{1s} \approx \frac{2\mu_{1s}}{T_0} = 5.22 \sigma_0 n_0^{-1/2} T_0^{-1}. \quad (13)$$

2.3.2. Long-Period Regime

In this regime, the analytical expressions for $\mathcal{A}_c, \mathcal{A}_s, \lambda$, and μ that we derived above no longer hold, and so we resort to simulations. To this end we create a synthetic data set consisting of Gaussian noise with $\sigma_0 = 100 \mu\text{as}$ (we simulate this measurement accuracy because future instruments such as FAME and Keck Interferometer will probably attain similar accuracies; Horner et al. 1999; van Belle et al. 1998). We sample the synthetic data at one month intervals for $T_0 = 12$ years. We explore orbital periods from 5 years to 100 years, choosing the interval between sampled periods so as to result in a one radian decrease in the total number of orbital cycles over the length of the observations,

$$\Delta\tau = \frac{\tau^2}{2\pi T_0}. \quad (14)$$

For each period, τ , we simulate $N = 1000$ data sets and carry out the least-squares fit. We set A_{c1} equal to the 10th highest value that arises. Clearly, 99% of fitted \mathcal{A}_c will lie below this value. Using the same method, we also determine the 99% confidence level for the other fitted parameters, which we denote by A_{s1} , λ_1 , and μ_1 .

We find that the values of the fitted parameters are in excellent agreement with the values predicted by Equations 6–9 in the short-period regime (Figure 1). In order to understand the behaviors of the fitted parameters in the long-period regime, we begin by examining how the covariance of the fitted parameters depends on period. We expect that in the short-period regime, all four parameters will be completely uncorrelated, since we observe many orbital periods and can thus easily distinguish the sinusoidal motion from the linear proper motion term and the constant offset term. This expectation is verified by the simulations (Figure 2).

In the long-period regime, in contrast, strong correlations may arise between the fitted parameters. From Figure 2, we conclude the following for the long-period regime:

1. \mathcal{A}_c and \mathcal{A}_s are correlated, and select orbital phases close to 0° .
2. \mathcal{A}_c and μ are anticorrelated.
3. \mathcal{A}_s and λ are anticorrelated.
4. \mathcal{A}_c and λ are uncorrelated (not shown in figure).
5. \mathcal{A}_s and μ are uncorrelated (not shown in figure).

Previous authors noted that these correlations would arise, and that the orbital phase would become important in the long-period regime (Black & Scargle 1982). However, neither they nor others have explored the full-implications of this fact. Below, we look into this issue in

more detail, and develop an analytical understanding of how the fitted parameters depend upon orbital period.

We now provide a physical explanation of the results displayed in Figure 2. When $\tau \ll T_0$, sinusoids with random phase can be fit to Gaussian data, where the amplitude of the sinusoids is constrained by the vertical scale of the data ($\sim \sigma_0$). However, when $\tau > T_0$, this is no longer necessarily the case. The maximum amplitude is obtained when a sine wave centered around $t = 0$ is fitted. This is because for $\tau > T_0$, $\sin(\pi T_0/\tau) \approx \pi T_0/\tau$, which can be completely absorbed into the linear proper motion term.

Specifically, the maximum amplitude of the sine wave that can be fitted is limited by how much $\sin(2\pi t/\tau)$ deviates from a straight line in the range from $t = [0, T_0/2]$. This deviation is given by

$$\frac{\pi T_0}{\tau} - \sin\left(\frac{\pi T_0}{\tau}\right). \quad (15)$$

We note that the maximal deviation occurs when $\tau \geq 3T_0/4$, and thus the long-period regime “begins” where $\tau = 3T_0/4$. The largest possible amplitude of the fitted sine wave (\mathcal{A}_s) in the long-period regime is that for which this deviation is approximately equal to the vertical scale of the noise ($\sim \sigma_0$). Since Equation 15 tells us the fractional observed amplitude, the real amplitude of the fitted sine is

$$A_{s1} = \frac{A_{1s}[4\pi/3 - \sin(4\pi/3)]}{\pi T_0/\tau - \sin(\pi T_0/\tau)}. \quad (16)$$

Here, A_{s1} is the value of $|\mathcal{A}_s|$ that is exceeded in 1% of least-squares fits to Gaussian noise, A_{1s} is the corresponding value of A_{s1} in the short-period regime (Equation 11), and the specific normalization is chosen so that at the boundary of the short and long-period regimes ($t = 3T_0/4$), A_{s1} is continuous.

We can understand the behavior of \mathcal{A}_c in the long-period regime using a similar analysis. Specifically, the maximum amplitude of a cosine wave centered around $t = 0$ is constrained by how much this cosine deviates from a constant in the interval $[0, T_0/2]$. Following the same lines as the analysis for \mathcal{A}_s , we find that this amplitude is given by

$$A_{c1} = \frac{2A_{1s}}{1 - \cos(\pi T_0/\tau)}. \quad (17)$$

Here, A_{c1} is the value of $|\mathcal{A}_c|$ that is exceeded in 1% of least-squares fits to Gaussian noise, A_{1s} is the corresponding value of A_{c1} in the short-period regime (Equation 11), and 2 is a normalization factor (chosen to enforce continuity between the short and long-period regimes). We note that in the long-period regime $\sin(x) \rightarrow x$ faster than $\cos(x) \rightarrow 1$, and thus the

covariance of the sinusoidal signal with the constant offset term is less significant than the covariance with the proper motion term.

In light of these analytical expressions for \mathcal{A}_c and \mathcal{A}_s , it is not difficult to find expressions for λ and μ . In particular, because the input data consists of Gaussian noise with a mean of zero, we know that λ and μ must be chosen so that the resultant fit is also, in the mean, zero. The anti-correlation of \mathcal{A}_c and μ and that of \mathcal{A}_s and λ confirm this expectation.

We must choose a λ that “cancels” the fitted sine-wave component. In the long-period regime, this condition can be expressed as $\mathcal{A}_s \sin(\omega t) \approx \mathcal{A}_s \omega t \sim \lambda t$, or $\lambda \sim \mathcal{A}_s/\tau$. However, because the data has some vertical scale, we must vertically “re-center” the data after subtracting \mathcal{A}_s/τ . Since the total vertical scale is $\sim 2\sigma_0$, we must add σ_0 after subtracting \mathcal{A}_s/τ . Thus, we expect that for $\tau \geq 3T_0/4$,

$$\lambda_1 = \lambda_{1s} \frac{3T_0}{4\tau} \left\{ 2 \frac{4\pi/3 - \sin(4\pi/3)}{\pi T_0/\tau - \sin(\pi T_0/\tau)} - 1 \right\}. \quad (18)$$

Similarly, μ is chosen to “cancel” the cosine component. Thus, μ is the negative cosine component (given by \mathcal{A}_c) plus σ_0 (where σ_0 is needed to reproduce the data, which is vertically centered around 0). Thus, for $\tau \geq T_0$,

$$\mu_1 = \mu_{1s} \left[\frac{4}{1 - \cos(\pi T_0/\tau)} - 1 \right]. \quad (19)$$

Equipped with the behaviors of \mathcal{A}_{c1} and \mathcal{A}_{s1} , we now know the analytical behavior of the Type I errors in the long-period regime. Specifically, the error ellipse within which 99% of fitted signals lie, ϵ_1 , is completely described: \mathcal{A}_{s1} gives the semi-major axis, and \mathcal{A}_{c1} gives the semi-minor axis.

Amplitude–Phase Analysis. The standard signal analysis usually focuses on the statistics of the orbital amplitude $\mathcal{A} = (\mathcal{A}_c^2 + \mathcal{A}_s^2)^{1/2}$. This is adequate when \mathcal{A}_c and \mathcal{A}_s are uncorrelated (e.g. in the short-period regime with adequate sampling). However, as can be seen in Figure 2, the \mathcal{A}_c – \mathcal{A}_s distribution becomes highly elliptical in the long-period regime. Thus in this regime it pays to undertake an analysis that utilizes amplitude and phase. The fact that the amplitude-phase ellipse (Figure 2) is significantly smaller than the amplitude-only circle in the long-period regime clearly indicates the superiority of an amplitude-phase approach. Therefore, we will use an amplitude-phase approach in the remainder of this discussion. See EK2001 for a more detailed comparison of amplitude-only and amplitude-phase approaches.

2.4. Type II Errors

In §2.3, we computed the probability of detecting an apparent signal generated purely by noise (i.e. Type I probabilities). We now consider Type II probabilities– the probability of failing to detect a genuine signal due to contamination by noise. To this end, we simulate a data set that consists of signal and noise:

$$\theta'(t_i) = \mathcal{A} \sin(\omega t_i + \phi) + N(t_i), \quad (20)$$

where \mathcal{A} is the amplitude of the signal, ϕ is the phase, and $N(t_i)$ is the Gaussian noise. We let ϕ be drawn from a uniform distribution in the interval $[0, 2\pi]$, an appropriate assumption for circular orbits. We choose an initial signal amplitude of $\sigma_0/2$, and then do $N = 1000$ least-squares fits (with the same parameters as in §2.3).

In §2.3, we showed that in the long-period regime, the \mathcal{A}_c – \mathcal{A}_s distribution is elliptical. In view of this, we define the Type I errors by an ellipse ϵ_1 ; this ellipse contains 99% of the zero-signal simulations (§2.3.2). In our analysis of Type II probabilities, we consider all least-squares fits (of the signal specified in Equation 20 to the model specified by Equation 4) that lie within ϵ_1 to be indistinguishable from those produced by noise. We increment the input signal amplitude until a certain fraction of fitted points lie outside of ϵ_1 . For example, the signal amplitude at which 99% of fitted points lie outside of ϵ_1 is denoted by A_{99} . Plots of A_{99} , A_{90} , and A_{50} (as a function of orbital period) are shown in Figure 3.

3. Face-On Orbits

In the case of face-on orbits, we have twice as many measurements as in the edge-on case, since there are two orbital dimensions. Thus, our model will contain both the x and y motion of the orbit:

$$\theta_x(t) = \mathcal{A}_c \cos(\omega t) + \mathcal{A}_s \sin(\omega t) + \lambda_x t + \mu_x, \quad (21)$$

$$\theta_y(t) = -\mathcal{A}_s \cos(\omega t) + \mathcal{A}_c \sin(\omega t) + \lambda_y t + \mu_y. \quad (22)$$

As above, $\mathcal{A}_c = \mathcal{A} \sin \phi$, $\mathcal{A}_s = \mathcal{A} \cos \phi$, $\vec{\lambda} = [\lambda_x, \lambda_y]$ is the proper motion, and $\vec{\mu} = [\mu_x, \mu_y]$ is the position offset.

Using the same parameters as in §2.2, we determine the unknown model parameters by minimizing

$$X^2 = \sum_{j=0}^{n_0-1} \{[\theta'_x(t_j) - \mathcal{A}_c \cos(\omega t_j) + \mathcal{A}_s \sin(\omega t_j) - \lambda_x t_j - \mu_x]^2 +$$

$$[\theta'_y(t_j) + \mathcal{A}_s \cos(\omega t_j) - \mathcal{A}_c \sin(\omega t_j) - \lambda_y t_j - \mu_y]^2\} \quad (23)$$

with respect to \mathcal{A}_c , \mathcal{A}_s , λ_x , λ_y , μ_x , and μ_y .

3.1. Type I Errors

Because a face-on orbit has two observable dimensions, the analysis of Type I errors will be somewhat more complicated than for the face-on case. First, we note that in the short-period regime where $\tau < T_0$, the least squares fit essentially has twice as many measurements to work with. Thus, we expect that A_{1s} will be $2^{-1/2}$ times its value for the edge-on case:

$$A_{1s} = 2.61\sigma = 2^{-1/2} \times 3.69 n_0^{-1/2} \sigma_0. \quad (24)$$

However, since λ and μ must be determined for each orbital dimension independently, μ_{1s} and λ_{1s} will still be given by Equations 12 and 13.

When $\tau > T_0$, the full amplitude of a cosine centered around $t = 0$ cannot be observed. However, in the case of face-on orbits, we can observe the full amplitude of the orbit in the orthogonal direction, since it is phase-shifted by 90° . The full amplitude of this sine wave can be observed until $\tau > 4T_0/3$ (to see this, find the value of τ for which $\cos(\pi T_0/\tau) = -\sin(\pi T_0/\tau)$).

For face-on orbits, the long-period regime begins when $\tau > 4T_0/3$, since it is here that the full amplitude of a sinusoid cannot be observed in either orbital dimension. Moreover, since the two dimensions are phase-shifted by 90° , we expect the expressions for A_{c1} and A_{s1} to be the same. Since $\sin(x) \rightarrow x$ faster than $\cos(x) \rightarrow 1$, the deviation of a cosine wave from unity will be the important constraint on the possible fitted amplitude. Thus, A_{c1} and A_{s1} are both given by Equation 17 in the long-period regime.

A potential complication is that at some point, we are gaining virtually no new information from one of the orbital dimensions (since the constraint on the size of a cosine is so much stronger than that on the size of a sine wave). So, we expect that at some period, our sensitivity will drop roughly by a factor of $2^{1/2}$, to reflect the fact that half of the measurements become useless. We model this behavior as follows:

$$A_{s1} = A_{c1} = \begin{cases} A_{1s} & \text{for } \tau < T_0 \\ \sqrt{2}A_{1s} & \text{for } T_0 < \tau < 4T_0/3 \\ \frac{2\sqrt{2}A_{1s}}{1-\cos(\pi T_0/\tau)} & \text{for } \tau > 4T_0/3 \end{cases} \quad (25)$$

As illustrated by Figure 4, this function is a good fit to the simulations.

Since A_{s1} now depends on the maximum amplitude of a cosine wave, rather than the amplitude of a sine wave, we must modify our expression for λ_1 accordingly. Specifically,

while the slope of a sine wave centered around $t = 0$ goes approximately as ωt , the slope of a cosine wave goes as $\omega^2 t^2$. Thus, we expect that the expression for λ_1 in the case of face-on orbits will differ from that for edge-on orbits by a factor of ω . Specifically, we find that for $\tau > T_0$,

$$\lambda_1 = \lambda_{1s} \left(\frac{T_0}{\tau} \right)^2 \left\{ 2 \frac{\pi - \sin \pi}{\pi T_0/\tau - \sin(\pi T_0/\tau)} - 1 \right\}. \quad (26)$$

This analytic function is shown along with the simulated data in Figure 4.

We expect that μ_1 will be the exactly the same as in the case of edge-on orbits, since the behavior of A_{c1} is unchanged. This expectation is confirmed by Figure 4.

From these analytic expressions for \mathcal{A}_c and \mathcal{A}_s , we see that the sensitivity of astrometric technique to face-on orbits is significantly better than that for edge-on orbits. This is well illustrated through a comparison of Figures 2 and 5. As discussed above, the Type I error ellipse, ϵ_1 , is defined as the ellipse in the \mathcal{A}_c – \mathcal{A}_s plane for which 99% of fitted parameters lie inside. In the case of edge-on orbits, this ellipse is very eccentric, since the semi-major axis is given by Equation 16 and the semi-minor axis is given by Equation 17 (Figure 2). In contrast, in the case of face-on orbits, ϵ_1 is a circle whose radius is given by Equation 25. Thus, for face-on orbits, we are equally sensitive to signals of arbitrary orbital phase.

3.2. Type II Errors

As in §2.4, we compute the probability that a real signal will not be detected due to contamination by noise. For a face-on orbit, we simulate the following data set:

$$\theta'_x(t_i) = \mathcal{A} \sin(\omega t_i + \phi) + N_x(t_i), \quad (27)$$

$$\theta'_y(t_i) = \mathcal{A} \cos(\omega t_i + \phi) + N_y(t_i), \quad (28)$$

Here, \mathcal{A} is the amplitude of the signal, ϕ is the (randomly-distributed) orbital phase, and $N(t_i)$ is the Gaussian noise. Since the sensitivity of astrometric technique to face-on orbits is better than for edge-on orbits by a factor of $2^{1/2}$ (in the short-period regime), we choose an initial signal amplitude of $\sigma_0/2^{3/2}$. We then do $N = 1000$ least-squares fits, with the same parameters as in §3.1.

Following our analysis of Type II errors in §2.4, we consider all least-squares fits (of the signal specified in Equations 27 and 28 to the model given by Equations 21 and 22) that lie within ϵ_1 to be indistinguishable from noise. The results of this analysis show that the sensitivity of the astrometric technique is much better for face-on orbits than for edge-on orbits (Figure 6).

4. Inclined Orbits

In the case of generally inclined orbits, we observe the full amplitude in one orbital dimension, but only $\sin i \times \mathcal{A}$ in the other dimension (where i is the orbital inclination angle). Labeling the dimension in which we measure the full amplitude by x , our model becomes

$$\theta_x(t) = \mathcal{A}_c \cos(\omega t) + \mathcal{A}_s \sin(\omega t) + \lambda_x t + \mu_x, \quad (29)$$

$$\theta_y(t) = -\sin i \mathcal{A}_s \cos(\omega t) + \sin i \mathcal{A}_c \sin(\omega t) + \lambda_y t + \mu_y. \quad (30)$$

As above, $\mathcal{A}_c = \mathcal{A} \sin \phi$, $\mathcal{A}_s = \mathcal{A} \cos \phi$, $\vec{\lambda}$ is the proper motion, and $\vec{\mu}$ is the position offset.

Using the same parameters for our data set as in §2.2, we determine the unknown model parameters by minimizing

$$X^2 = \sum_{j=0}^{n_0-1} \{[\theta'_x(t_j) - \mathcal{A}_c \cos(\omega t_j) - \mathcal{A}_s \sin(\omega t_j) - \lambda_x t_j - \mu_x]^2 +$$

$$[\theta'_y(t_j) + \sin i \mathcal{A}_s \cos(\omega t_j) - \sin i \mathcal{A}_c \sin(\omega t_j) - \lambda_y t_j - \mu_y]^2\} \quad (31)$$

with respect to \mathcal{A}_c , \mathcal{A}_s , λ_x , λ_y , μ_x , and μ_y .

4.1. Type I Errors

In the short-period regime where $\tau < T_0$, the least squares fit essentially has twice as many measurements with which to work, although half of the measurements are less sensitive. Thus, we expect that Type I errors will be somewhere between those for the edge-on and face-on cases. However, for simplicity, we will simply use the expressions from the face-on case.

As above, A_{c1} is given by Equation 17 in the long-period regime, since we can always observe the full amplitude of a cosine wave in one orbital dimension. However, A_{s1} will be different than in the face-on case, since the cosine wave cannot be measured as accurately in the other orbital dimension. Thus, we expect that in the long-period regime, A_{s1} will be stretched relative to A_{c1} . For orbits with inclination angles close to zero, there is essentially no information from the second orbital dimension, and thus A_{s1} is given by Equation 16. However, for inclination angles significantly greater than zero, the information from the second orbital dimension becomes important, and A_{s1} is limited by the lower-amplitude cosine wave in this second dimension. Specifically, A_{s1} is A_{c1} stretched by $1/\sin i$. Thus, we

have an expression for the aspect ratio of ϵ_1 as a function of inclination angle:

$$\frac{A_{s1}}{A_{c1}} = \min \left(\frac{1}{\sin i}, \left[\frac{A_{c1}}{A_{s1}} \right]_{\text{edge}} \right). \quad (32)$$

As an example, we determine the Type I errors for a 45° -inclined orbit. In this case, $A_{s1} = A_{c1}/\sin i = 2^{1/2}A_{c1}$ (Figure 7). Since A_{s1} is increased by $2^{1/2}$ from the face-on case, λ_1 must be similarly increased:

$$\lambda_1 = \sqrt{2}\lambda_{1s} \left(\frac{T_0}{\tau} \right)^2 \left\{ 2 \frac{\pi - \sin \pi}{\pi T_0/\tau - \sin(\pi T_0/\tau)} - 1 \right\}. \quad (33)$$

We expect that μ_1 will be the exactly the same as in the case of edge-on orbits, since the behavior of A_{c1} is unchanged. Analytic functions for the parameters are shown along with the simulated data in Figure 8.

4.2. Type II Errors

As in §2.4 we compute the probability that a real signal will not be detected due to contamination by noise. For inclined orbits, we simulate the following data set:

$$\theta'_x(t_i) = \mathcal{A} \sin(\omega t_i + \phi) + N_x(t_i), \quad (34)$$

$$\theta'_y(t_i) = \sin i \mathcal{A} \cos(\omega t_i + \phi) + N_y(t_i), \quad (35)$$

Here, \mathcal{A} is the amplitude of the signal, ϕ is the (randomly-distributed) orbital phase, and $N(t_i)$ is the Gaussian noise. We choose an initial signal amplitude, and do $N = 1000$ least-squares fits, with the same parameters as in §3.2.

Following our analysis of Type II errors in §2.4, we consider all least-squares fits (of the signal specified in Equations 34 and 35 to the model given by Equations 29 and 30) that lie within ϵ_1 to be indistinguishable from noise. The results of this analysis for a 45° -inclined orbit are shown in Figure 9.

5. Caveats and Conclusions

As in our earlier analysis of the sensitivity of the radial velocity technique (EK2001), the analysis presented here is based on frequentist statistics. However, the importance of the Bayesian approach is gradually being recognized in astronomy. Berger & Delampady

(1987) point out that the probability of extreme events predicted by the frequentist approach (which is what we have essentially computed) is rosier than is warranted. Thus, given a mix of stars (with and without planets), the frequentist tail criterion of say 1% (e.g. ϵ_1) is likely to underestimate the fraction of false detections that are expected to occur in population analyses. These criticisms notwithstanding, we have pursued the frequentist approach because of (1) its conceptual simplicity, (2) its ease of use, (3) our own familiarity, and (4) our lack of familiarity with the Bayesian approach.

We also acknowledge that our treatment of the statistics was not always completely rigorous. Specifically, when one orbital dimension becomes much more sensitive than the other, we simply ignore the data from the other dimension. Inclusion of this less sensitive dimension in the analysis is likely to lead to a small improvement in the overall sensitivity. We feel that this statistical analysis is beyond the scope of this paper, and will not lead to any meaningful modifications of the results derived above.

A final caveat is that in this analysis, we have assumed that the orbital inclination angle is known *a priori*. In general, this is not the case, and the inclination angle must be determined simultaneously with the rest of the orbital parameters (using a non-linear least-squares fitting method). While one expects that all of the sensitivities in this paper are slightly under-estimated as a result, it is clear that the qualitative behavior of the sensitivity in the long-period regime is unaffected.

Despite the fact that our analysis can be improved upon in some areas, this work provides an accurate analytic description of the sensitivity of the astrometric technique in detecting outer planets. Moreover, we have understood, both qualitatively and quantitatively, how the sensitivity improves as the orbital inclination angle is increased. Of specific importance is the fact that in the long-period regime the sensitivity of astrometric technique to face-on orbits is more than $2^{1/2}$ times better the sensitivity to edge-on orbits, due to the orthogonal information supplied by the two orbital dimensions.

REFERENCES

- Berger, J.O., & Delampady, M., 1987, *Statistical Sci.*, 2(3), 317
- Black, D.C., & Scargle, J.D., 1982, *Ap. J.*, 263, 854
- Boss, A.P., 1995, *Science*, 267, 360
- Danner, R., & Unwin, S., 1999, *Space Interferometry Mission Book*
- Eisner, J.A., & Kulkarni, S.R., 2001, *Ap. J.*, 550, 871

- Horner et al., 1999, in IAU Colloquium 176, The Impact of Large-Scale Surveys on Pulsating Star Research, eds. L. Szabados & D. Kurtz (ASP Conference Series) in press.
- Marcy, G.D., Cochran, W.D., & Mayor, M., 2000, Protostars and Planets IV, eds Mannings, V., Boss, A.P., & Russell, S. S., University of Arizona Press, p. 1285
- Nelson, A.F., & Angel, J.R.P., 1998, Ap. J., 500, 940
- Scargle, J.D., 1982, Ap. J., 263, 835
- van Belle, G.T., Boden, A.F., Colavita, M.M., et al., 1998, SPIE, 3350, 362

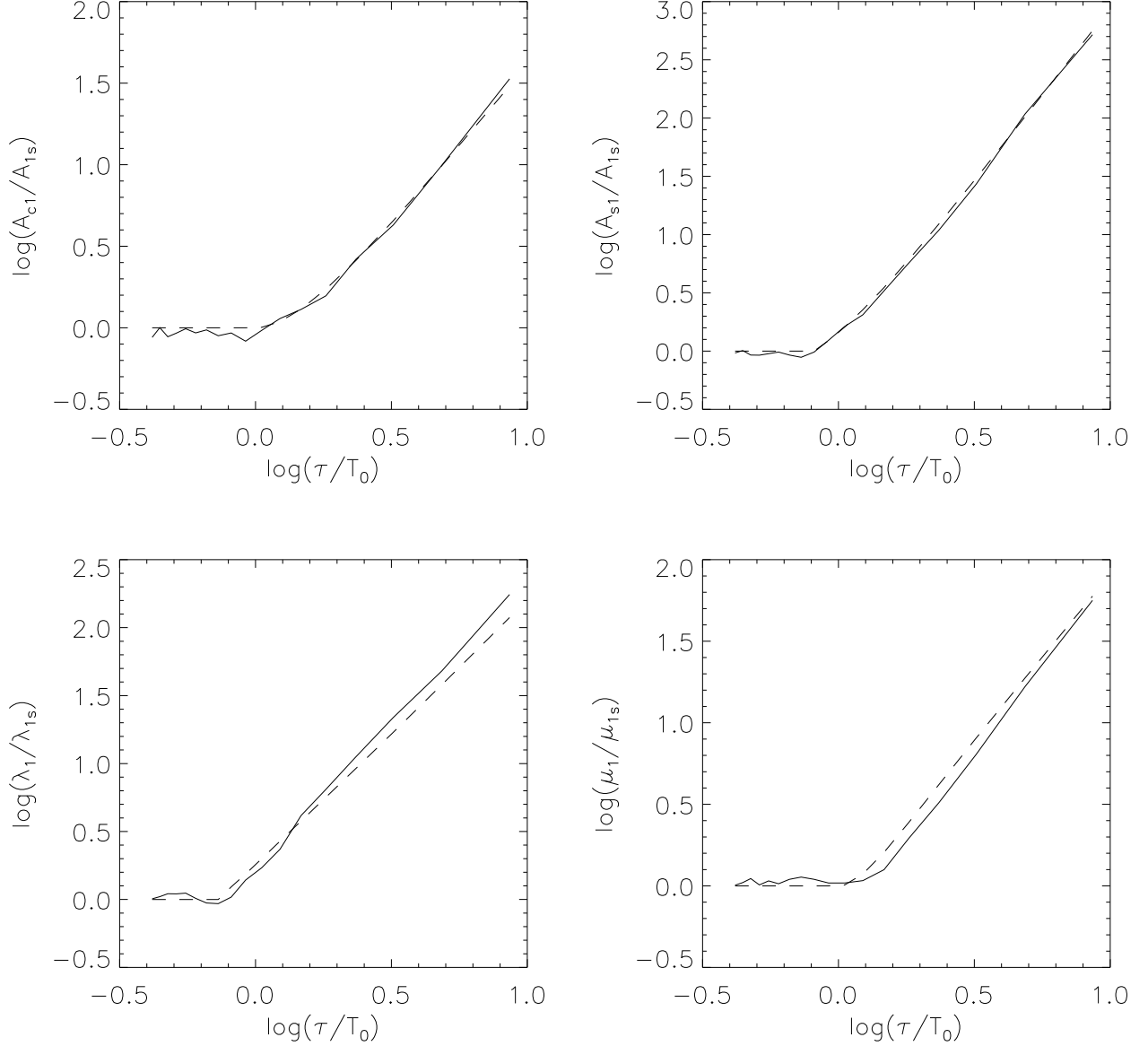


Fig. 1.— Illustration of how the fitted parameters depend on orbital period in the case of edge-on orbits. The solid lines indicate the 99th percentile values of the orbital parameters \mathcal{A}_c , \mathcal{A}_s , λ , and μ . Here, we simulated $N = 1000$ data sets with Gaussian noise of zero mean and $\sigma_0 = 100 \mu\text{as}$. Data were sampled at one-month intervals for $T_0 = 12$ years. The dashed lines show the analytic estimates predicted by Equations 16–19.

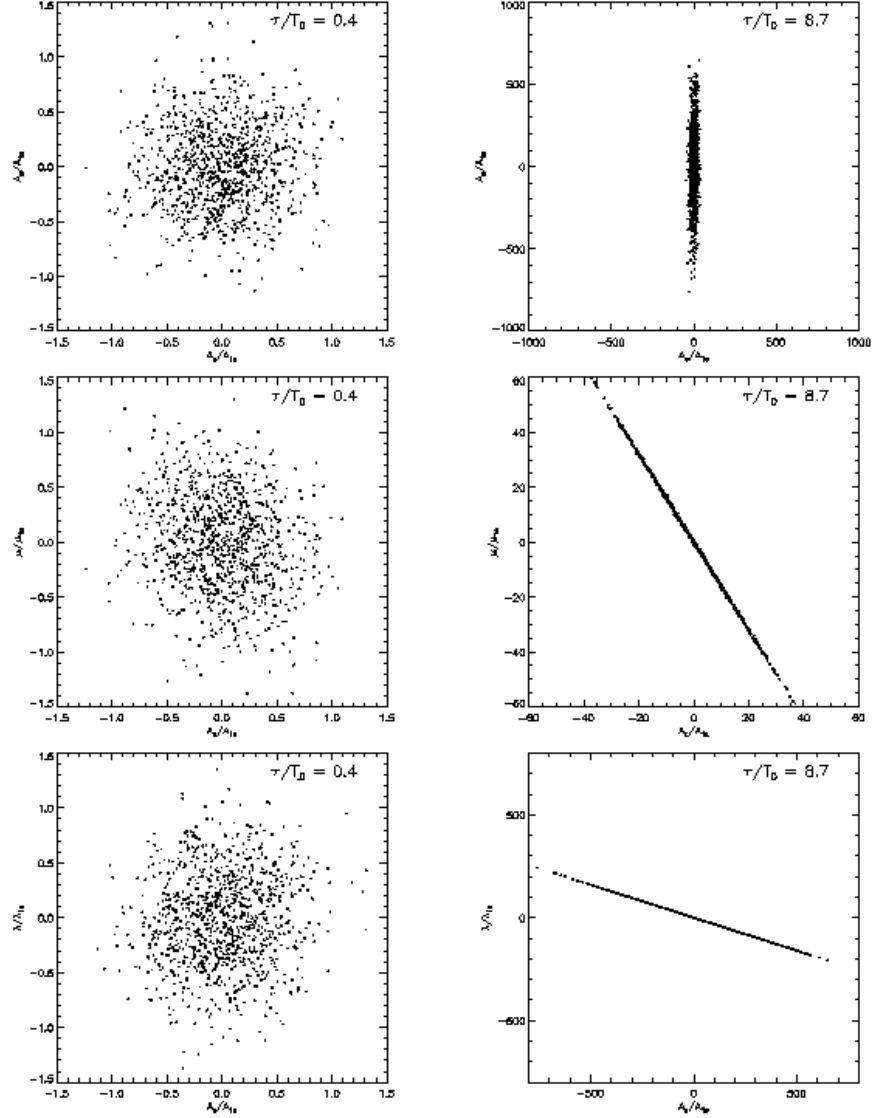


Fig. 2.— Correlations between fitted parameters for edge-on orbits in the short- and long-period regimes. Each dot represents one out of the $N = 1000$ simulations. The duration of the astrometric monitoring is $T_0 = 12$ yr. In the short-period regime, $\tau \ll T_0$, all of the orbital parameters are uncorrelated. In the long-period regime, strong correlations are seen. In particular, orbital phases of approximately 0° are preferred (i.e. the Type I error ellipse has a large aspect ratio), \mathcal{A}_c and μ are anticorrelated, and \mathcal{A}_s and λ are anti-correlated.

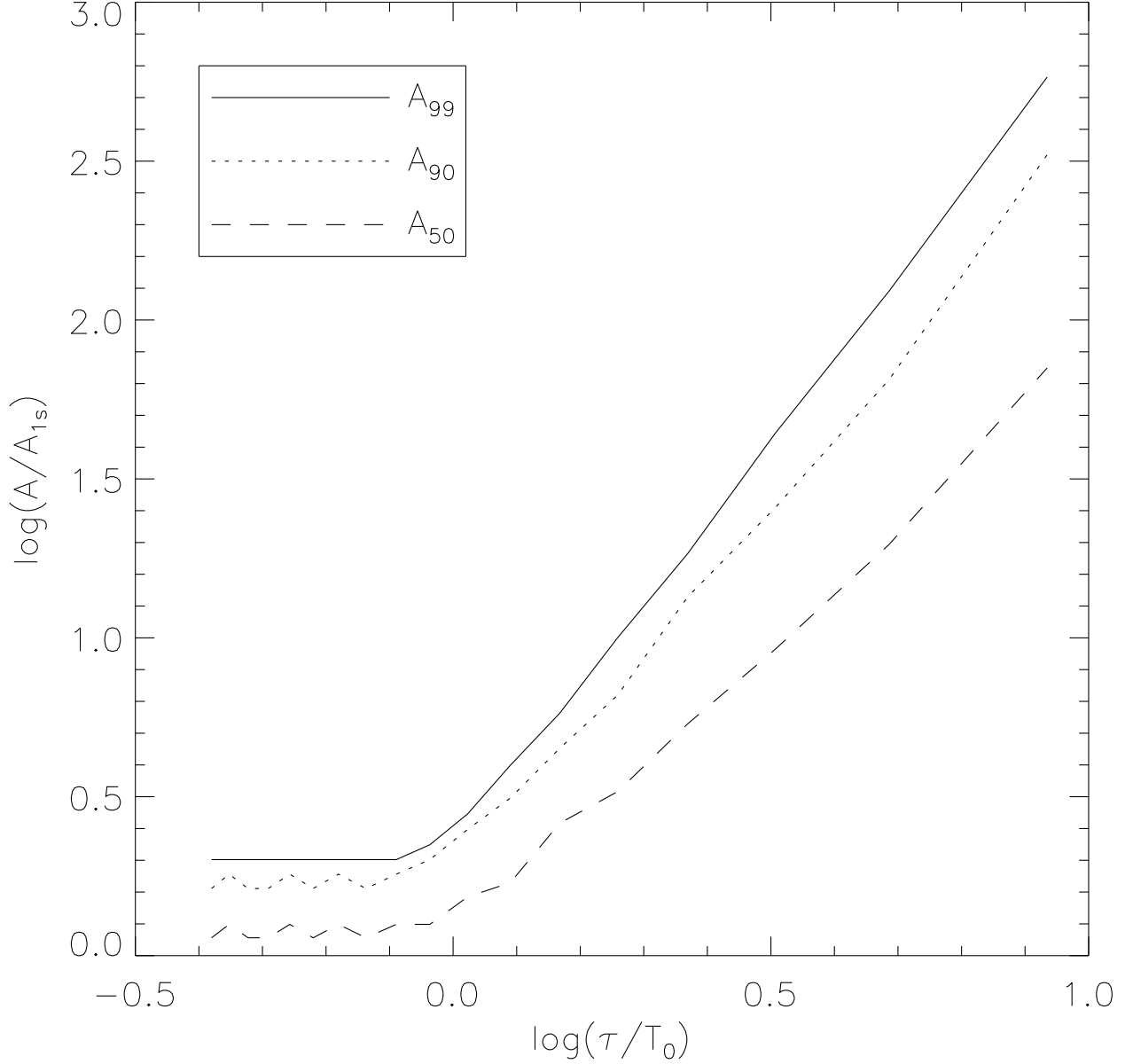


Fig. 3.— Plots of A_{99} , A_{90} , and A_{50} and a function of orbital period, for edge-on orbits. A_{99} is the signal amplitude necessary such that least-squares fits to data containing a genuine signal plus Gaussian noise will yield detections 99% of the time. We simulated $N = 1000$ data sets sampled at one-month intervals for $T_0 = 12$ years. The data sets consist of Gaussian noise (with zero mean and $\sigma_0 = 100 \mu\text{as}$) plus signal; the phase of the signal was assumed to be randomly and evenly distributed over the range $[0, 2\pi]$.

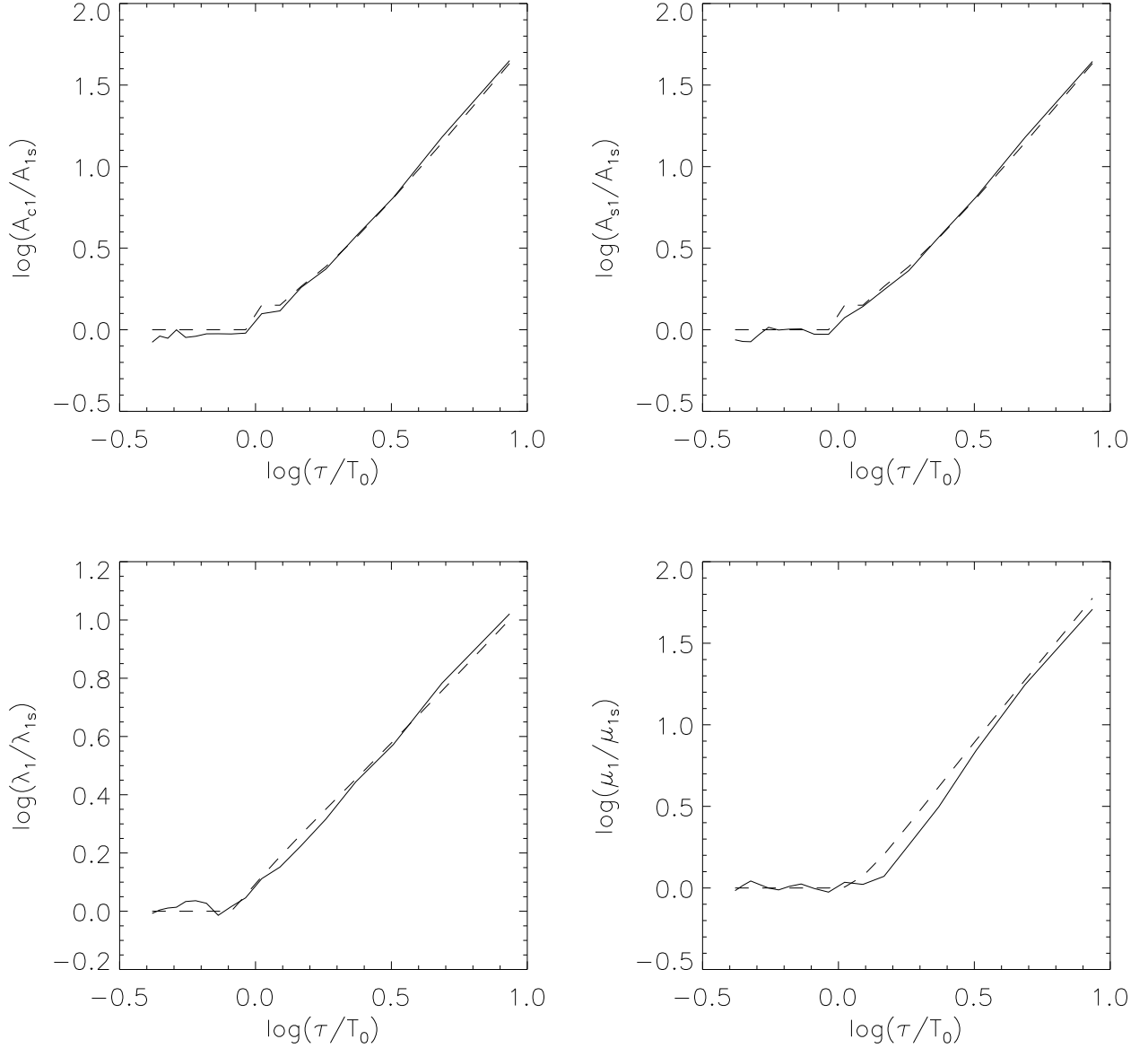


Fig. 4.— Illustration of how the fitted parameters depend on orbital period in the case of face-on orbits. The solid lines indicate the 99th percentile values of the orbital parameters \mathcal{A}_c , \mathcal{A}_s , λ , and μ , and the dashed lines show the analytic estimates predicted in §3.1. See Figure 1 for details of the simulations.

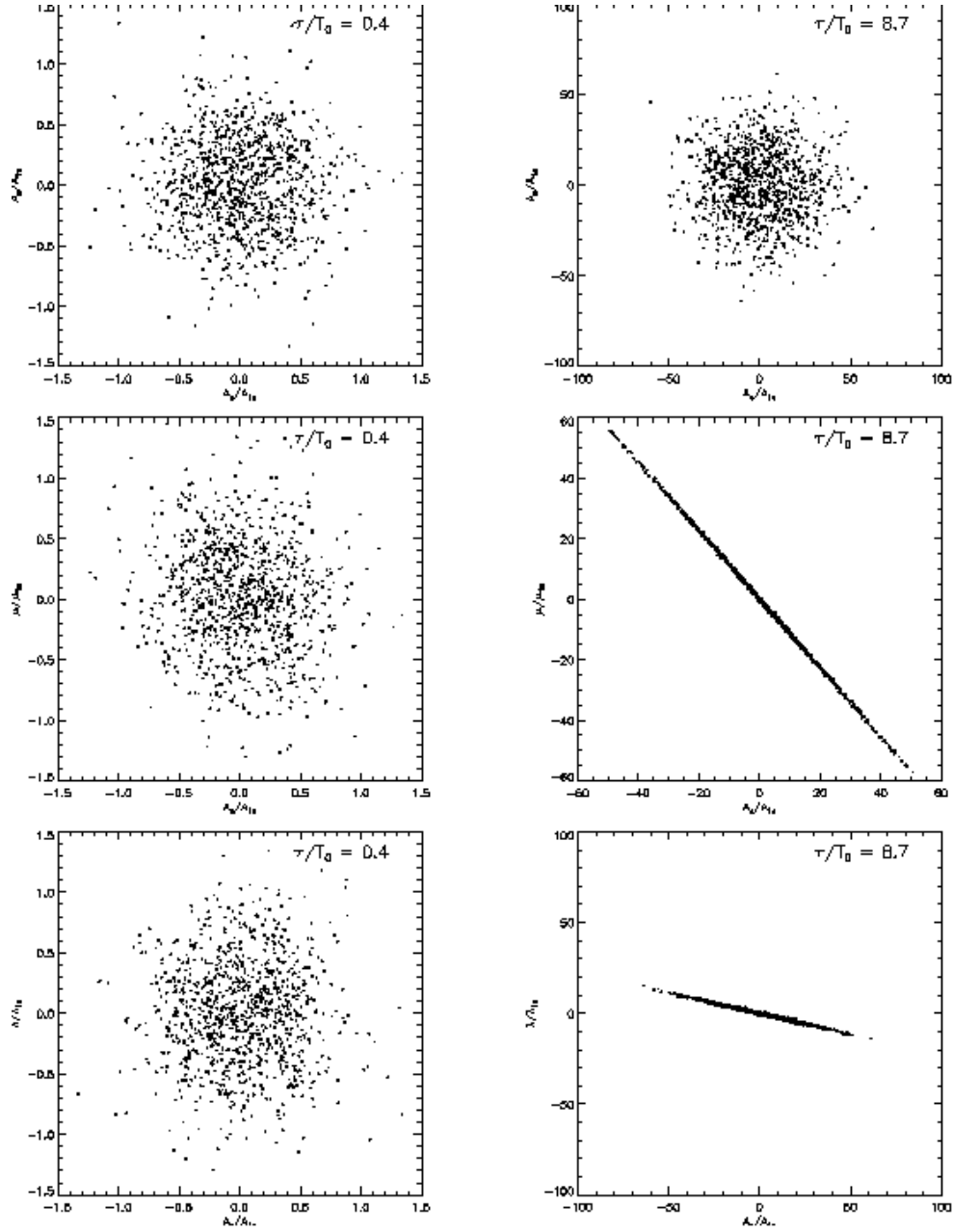


Fig. 5.— Correlations between fitted parameters for face-on orbits. Each dot represents one out of the $N = 1000$ simulations. The duration of the astrometric monitoring is $T_0 = 12$ yr. In the case of face-on orbits, we see that \mathcal{A}_c and \mathcal{A}_s remain uncorrelated in the long-period regime, and thus the aspect ratio of the Type I error ellipse ϵ_1 is unity.

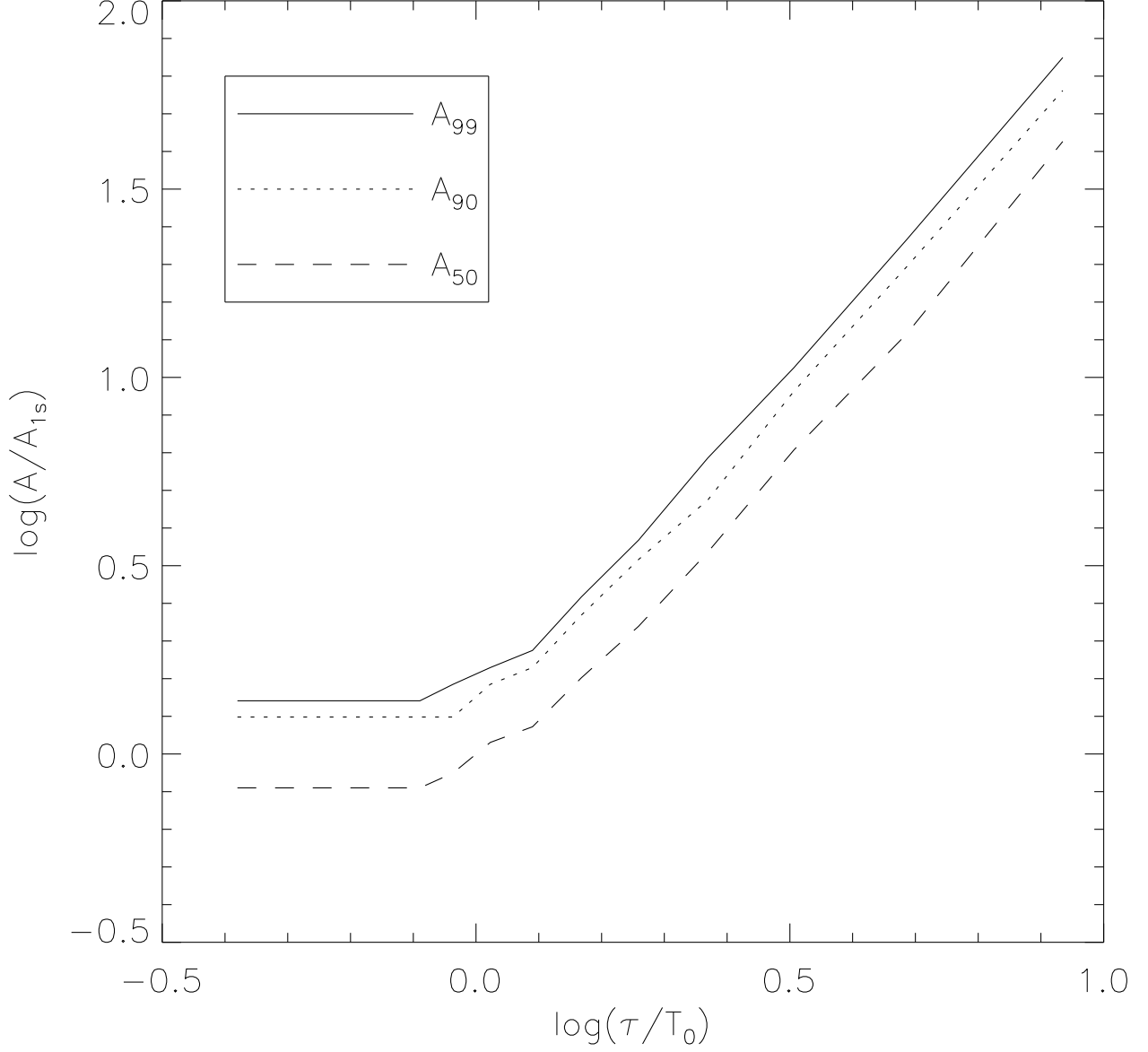


Fig. 6.— Plots of A_{99} , A_{90} , and A_{50} as a function of orbital period, in the case of face-on orbits. A_{99} is the signal amplitude necessary such that least-squares fits to data containing a genuine signal of random phase plus Gaussian noise will yield detections 99% of the time. See Figure 3 for details of the simulations.

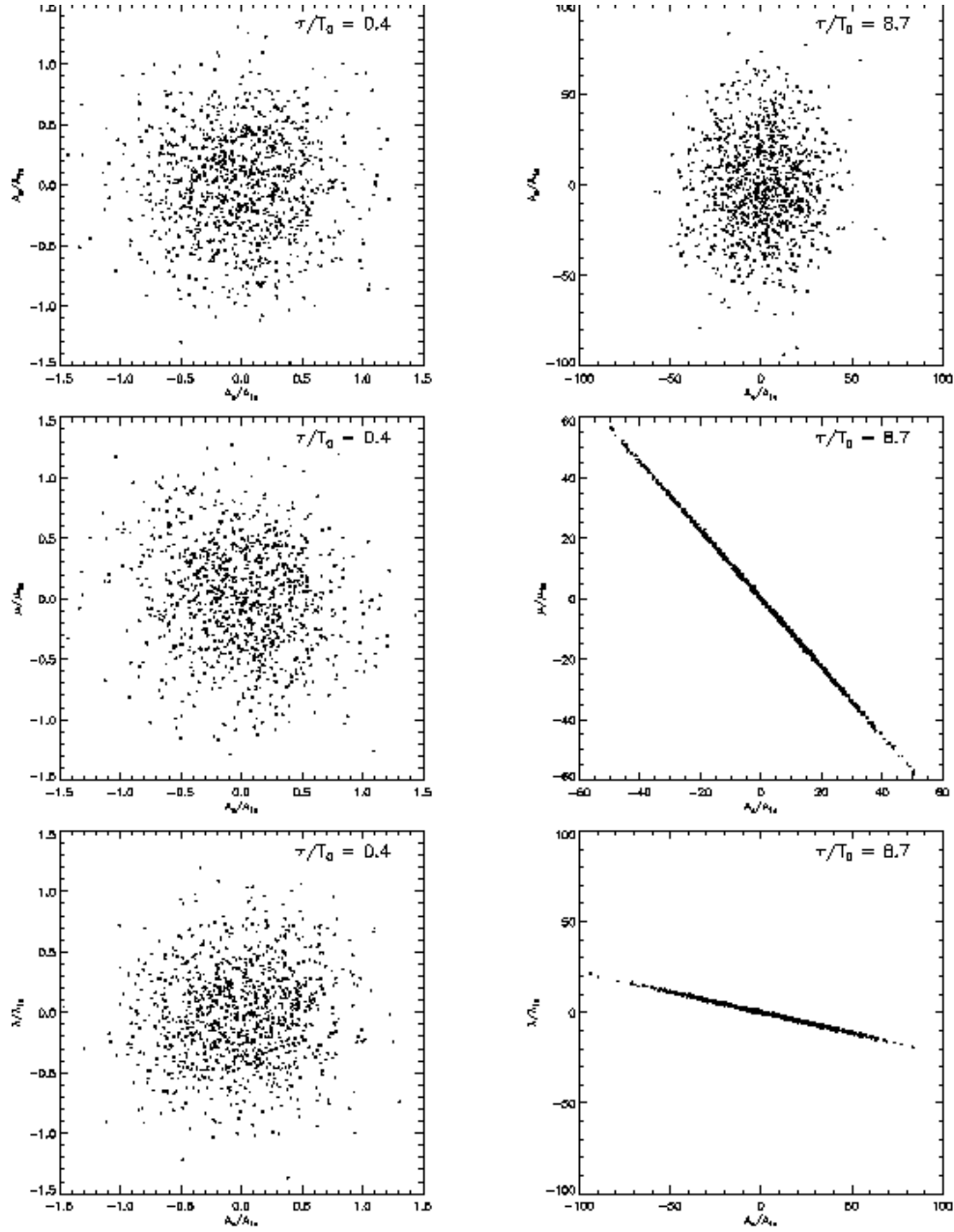


Fig. 7.— Correlations between fitted parameters for 45° -inclined orbits. Each dot represents one out of the $N = 1000$ simulations. The duration of the astrometric monitoring is $T_0 = 12$ yr. In the case of 45° -inclined orbits, we see that the aspect ratio of the Type I error ellipse ϵ_1 is $2^{1/2}$ in the long-period regime.

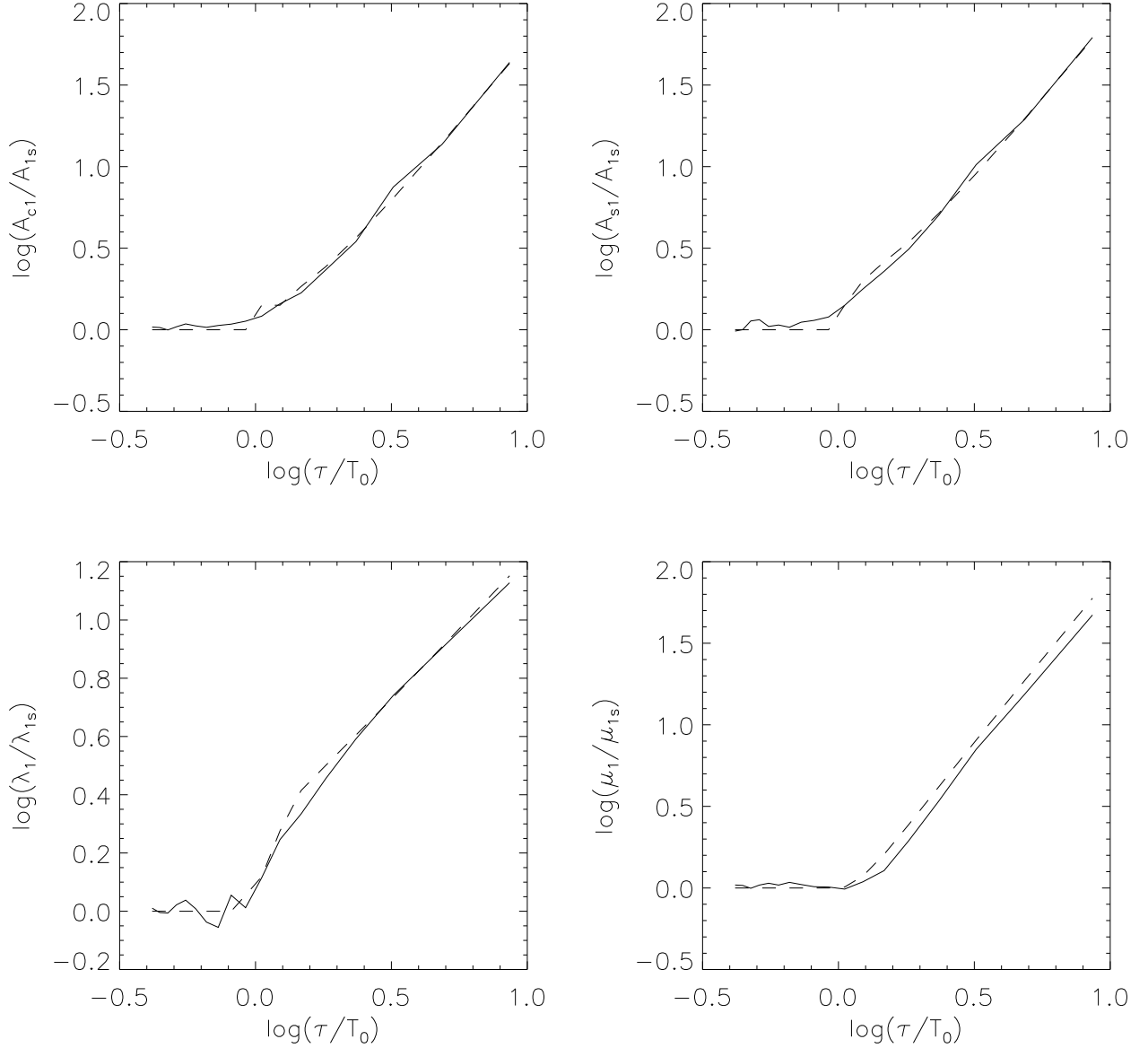


Fig. 8.— Illustration of how the fitted parameters depend on orbital period in the case of 45°-inclined orbits. The solid lines indicate the 99th percentile values of the orbital parameters \mathcal{A}_c , \mathcal{A}_s , λ , and μ , and the dashed lines show the analytic estimates predicted in §4.1. See Figure 1 for details of the simulations.

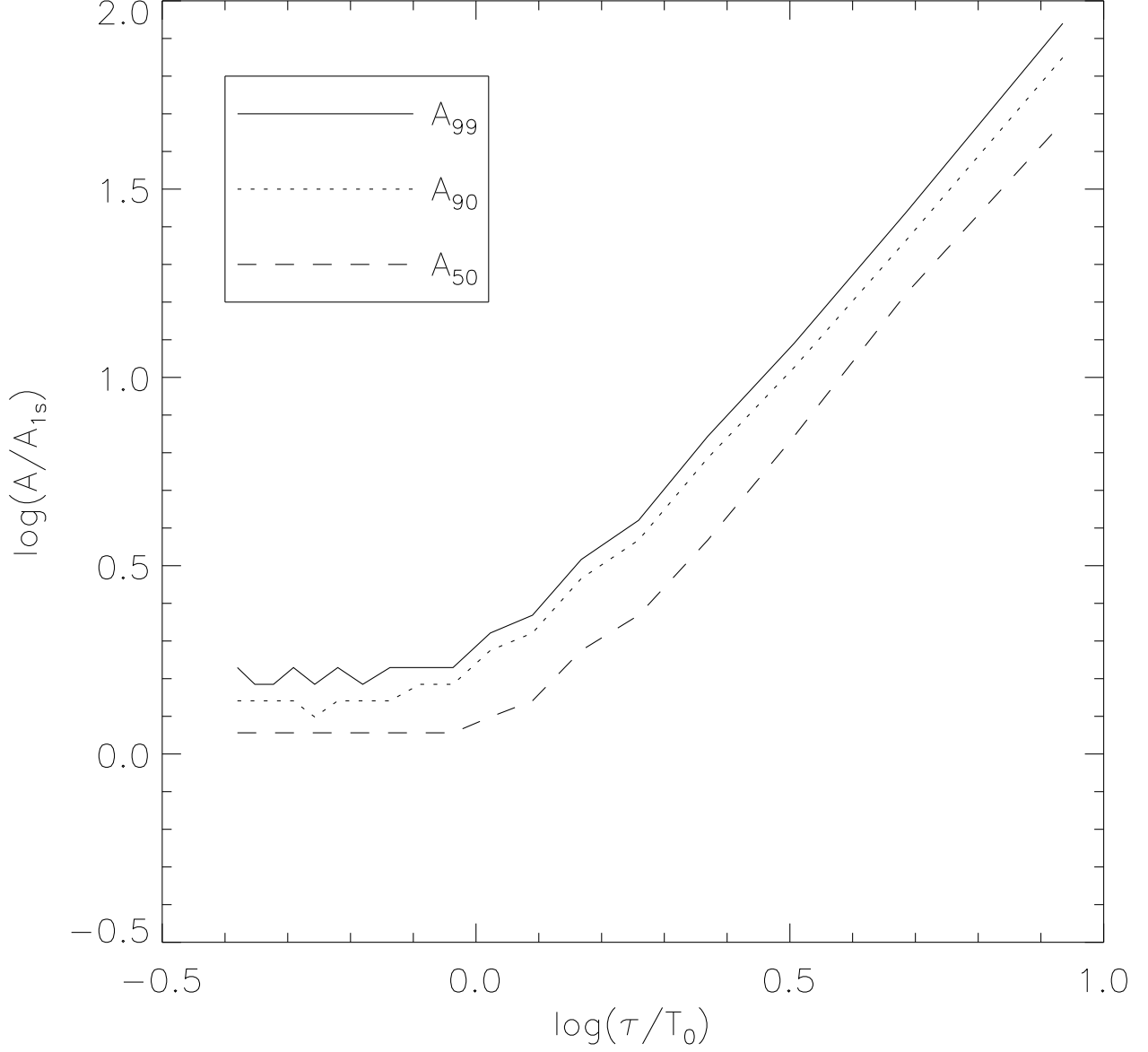


Fig. 9.— Plots of A_{99} , A_{90} , and A_{50} as a function of orbital period, in the case of 45° -inclined orbits. A_{99} is the signal amplitude necessary such that least-squares fits to data containing a genuine signal of random phase plus Gaussian noise will yield detections 99% of the time. See Figure 3 for details of the simulations.